Low doses of zeolitic imidazolate framework-8 nanoparticles alter the actin organization and contractility of vascular smooth muscle cells

Divya Kota[1,3,†], **Lin Kang**[1,3,†], **Alex Rickel**[2,3], **Jinyuan Liu**[1,3], **Steve Smith**[1,3], **Zhongkui Hong**[2,3,*], **Congzhou Wang**[1,3,*]

[1] Nanoscience and Nanoengineering, South Dakota School of Mines and Technology, 501 East Saint Joseph Street, Rapid City, South Dakota, USA, 57701

[2] Biomedical Engineering, University of South Dakota, 4800 N Career Avenue, Sioux Falls, South Dakota, USA, 57107

[3] BioSystems Networks & Translational Research (BioSNTR), 501 East Saint Joseph Street, Rapid City, South Dakota, USA, 57701

Abstract

Zeolitic imidazolate framework-8 (ZIF-8) nanoparticles have emerged as a promising platform for drug delivery and controlled release. Considering most ZIF-8 nanoparticle drug carriers are designed to be administered intravenously, and thus would directly contact vascular smooth muscle cells (VSMCs) in many circumstances, the potential interactions of ZIF-8 nanoparticles with VSMCs require investigation. Here, the effects of low doses of ZIF-8 nanoparticles on VSMC morphology, actin organization, and contractility are investigated. Two nanoscale imaging tools, atomic force microscopy, and direct stochastic optical reconstruction microscopy, show that even at the concentrations (12.5 and 25 μg/ml) that were deemed "safe" by conventional biochemical cell assays (MTT and LDH assays), ZIF-8 nanoparticles can still cause changes in cell morphology and actin cytoskeleton organization at the cell apical and basal surfaces. These cytoskeletal structural changes impair the contractility function of VSMCs in response to Angiotensin II, a classic vasoconstrictor. Based on intracellular zinc and actin polymerization assays, we conclude that the increased intracellular Zn^{2+} concentration due to the uptake and dissociation of ZIF-8 nanoparticles could cause the actin cytoskeleton dis-organization, as the elevated Zn^{2+} directly disrupts the actin assembly process, leading to altered actin organization such as branches and networks. Since the VSMC phenotype change and loss of contractility are fundamental to the development of atherosclerosis and related cardiovascular diseases, it is worth

*To whom correspondence should be addressed: zhongkui.hong@usd.edu, congzhou.wang@sdsmt.edu.
†D. Kota and L. Kang contributed equally to this work.

noting that these low doses of ZIF-8 nanoparticles administered intravenously could still be a safety concern in terms of cardiovascular risks. Moving forward, it is imperative to re-consider the "safe" nanoparticle dosages determined by biochemical cell assays alone, and take into account the impact of these nanoparticles on the biophysical characteristics of VSMCs, including changes in the actin cytoskeleton and cell morphology.

Keywords

zeolitic imidazolate framework-8 nanoparticles; vascular smooth muscle cells; cell morphology; actin cytoskeleton; contractility

Introduction

Metal-organic frameworks (MOFs), a class of crystalline hybrid materials consisting of metal ions or clusters coordinated to organic ligands, have received increased interest in the field of nanomedicine.[1–6] In particular, zeolitic imidazolate framework-8 (ZIF-8) nanoparticles, as a subclass of MOFs, have emerged as a promising platform for drug delivery and controlled release, thanks to their mild encapsulation conditions,[7–10] excellent drug loading and stabilization capacity,[11–15] and pH-responsive drug release under slightly acidic environments.[16, 17] So far, ZIF-8 nanoparticles have been used to encapsulate and deliver small anticancer drugs such as doxorubicin and tirapazamine,[17, 18] peptides and proteins such as insulin and glucose oxidase for diabetes,[19, 20] and nucleic acids for gene therapy.[21, 22] It is widely accepted that ZIF-8 nanoparticles have relatively low cytotoxicity and good biocompatibility. As with other nanoparticles, the typical procedure to determine the "safe dose" of ZIF-8 nanoparticles is through biochemical cell viability assays (e.g., MTT assay). Typically, cells are incubated with a series of concentrations of ZIF-8 nanoparticles for a short period of time (4–48 hours), if more than 90% of the cells remain viable, the concentration is considered "safe".[16, 17, 23] However, recent studies in the nanotoxicology field indicate that some metal-based nanoparticles can induce abnormalities in the actin cytoskeleton and cell morphology, at lower concentrations than those which show changes in cell viability. For instance, Liang and Parak's study showed that gold nanoparticles altered the actin organization and cell morphology at lower nanoparticle concentrations, than those that led to the onset of the reduced cell viability.[24] Another pioneering work by Setyawati, Leong and co-authors demonstrated that titanium dioxide nanoparticles can induce morphological changes and increased mobility for colorectal cancer cells at the "safe" concentrations pre-determined from cell viability assays.[25] Considering the ZIF-8 nanoparticles are metal-containing, and the increased interest in their applications for nanomedicine, we began to ask whether ZIF-8 nanoparticles at "safe" concentrations can alter cell morphology, which could be an overlooked adverse effect of ZIF-8 nanoparticles.

Different types of cells have been employed to investigate the cytotoxicity of ZIF-8 using biochemical cell viability assays. Early studies indicated that ZIF-8 nanoparticles had half maximal effective concentrations (EC50, the concentration causing 50% cell viability) of 45 μg/ml and 100 μg/ml on human breast cancer cells and human cervical cancer cells,

respectively.[23, 26] More recently, a systematic study demonstrated that ZIF-8 microparticles had no significant cytotoxicity up to a threshold value of 30 μg/ml on different cell lines including mouse macrophages, mouse embryo fibroblasts, human bone fibroblasts, human kidney epithelial cells, human keratinocyte epithelial cells, and human breast cancer cells.[27] However, it should be noted that the impact of ZIF-8 nanoparticles on vascular cells including vascular smooth muscle cells and endothelial cells are still unclear, even though most ZIF-8 nanoparticles as drug carriers are designed to be administered intravenously and therefore could directly contact cells lining blood vessels. Although considerable effort has been made in studying the effects of metal-based nanoparticles on vascular endothelial cells (i.e., the monolayer covering the lumen of blood vessels),[28–31] there is limited information available on whether metal-based nanoparticles would affect the vascular smooth muscle cells underneath the endothelium. Herein, we chose to focus on the impact of ZIF-8 nanoparticles on vascular smooth muscle cells (VSMCs) based on the following justifications: (i) A number of risk factors such as hypertension, diabetes, mechanical damage, smoking, aging, inflammation, cancer, and viral infection could result in endothelial dysfunction and its increased permeability,[32–35] thereby directly exposing underlying VSMCs to the nanoparticles; (ii) Accumulating evidence suggests that metal-based nanoparticles could lead to endothelial leakage at endothelial cell junctions,[28, 36] which could cause the accumulation of nanoparticles in VSMCs; and (iii) Under various stimuli, VSMCs tend to undergo phenotypic change, from contractile to synthetic phenotype, which could initiate atherosclerosis, a main cause of heart attack, stroke, and heart failure.[37–39] With these considerations, it is important to evaluate the impact of ZIF-8 nanoparticles on VSMCs before applying them to treat diseases such as cancers and diabetes, in order to ascertain whether or not ZIF-8 nanoparticles could increase the risk of cardiovascular diseases.

In this study, we aim at the effects of low doses of ZIF-8 nanoparticles on VSMCs at the level of cell actin cytoskeleton and cell morphology, both of which are important structural characteristics that determine the main function of VSMCs: regulating vascular tones through the cell contraction.[40, 41] First, biochemical cell assays were conducted to identify the accepted "safe" concentrations of ZIF-8 nanoparticles. Under these "safe" concentrations, atomic force microscopy (AFM) was performed to investigate the effects of ZIF-8 nanoparticles on VSMC morphology, actin cytoskeleton at the cell apical surfaces, and cell mechanical properties at the single cell level. Meanwhile, direct stochastic optical reconstruction microscopy (dSTORM), a super-resolution fluorescence imaging approach, was utilized to examine the effect of ZIF-8 nanoparticles on VSMC actin organization at the cell basal layers. The results showed that, even at the "safe" concentrations, ZIF-8 nanoparticles caused changes in actin cytoskeleton at the cell apical and basal surfaces, and the cell morphology. These changes further impaired the contractility of VSMCs in response to a classic vasoconstrictor (Angiotensin II). We hypothesized that the increased intracellular zinc concentration due to the uptake and dissociation of ZIF-8 nanoparticles could cause the actin cytoskeleton disorganization, and this hypothesis was tested by an actin polymerization assay and AFM imaging. Overall, the implications of our findings could be important for in vivo applications that would administer ZIF-8 nanoparticles intravenously, as even low doses of ZIF-8 nanoparticles may promote the risks of cardiovascular diseases. Moving forward, it

is imperative to re-consider the "safe" nanoparticle dosages that are determined by the biochemical cell assays alone, and take into account the impact of nanoparticles on the actin cytoskeleton and cell morphology, especially for vascular smooth muscle cells.

Methods

Materials

DMEM/F-12 culture medium, penicillin, streptomycin, PBS buffer, and DPBS buffer were purchased from Gibco. HEPES, Sodium pyruvate, L-glutamine, BlockAid buffer, Alexa Fluor 568 phalloidin, DTT, Leibowitz-15 culture medium, and pure collagen-I were purchased from Thermo Fisher Scientific. Fetal bovine serum (FBS) was purchased from Atlanta Biologicals. Zinc nitrate hexahydrate (99%), 2-methylimidazole (99%), fluorescein free acid (FITC), MTT, glucose, catalase, glucose oxidase, magnesium chloride, MES hydrate, EGTA, glutaraldehyde, Triton X-100, sodium chloride, sodium borohydride, and cysteamine (MEA) were purchased from Sigma-Aldrich. Paraformaldehyde (PFA) was purchased from Alfa Aesar. Glass-bottom dishes were purchased from WPI. 96-well plates were purchased from Corning. G-actin from rabbit skeletal muscle, ATP, G-buffer, and P-buffer were purchased from Cytoskeleton Inc.

ZIF-8 crystals synthesis and characterization

For the ZIF-8 nanoparticles (60 nm in diameter),150 mg of zinc nitrate hexahydrate and 330 mg of 2-methylimidazole were measured and transferred into a clean scintillation vial and glass tube, respectively. 7.15 ml of HPLC grade methanol was used to dissolve contents in both containers separately. For FITC loaded ZIF-8 nanoparticles, 30 μl of 2 mg/ml FITC dissolved in methanol was added to the scintillation vial containing the zinc nitrate solution, and the solution showed a faint yellow color. The scintillation vial was added with a magnetic stirrer bar and put on a stir plate, followed by the addition of 2-methyl imidazole solution. After 5 min vigorous stiring, the mixture solution turned turbid, indicating the formation of ZIF-8 nanoparticles. The ZIF-8 nanoparticles were collected and washed three times in methanol by centrifugation (7000 rpm, 10 min each time). Finally, the ZIF-8 nanoparticles were dried at 60°C for 24 h, weighed, and suspended in 5 ml of methanol for storage. The morphology of the ZIF-8 nanoparticles was characterized using transmission electron microscope (TEM-JEOL JEM 2100 LaB$_6$ TEM at 200 keV). The X-ray diffraction (XRD) measurements of the dried ZIF-8 powder were recorded on a Bruker D8-Advance X-ray powder diffractometer using Cu Kα radiation (λ = 1.5406 Å) with scattering angles (2θ) of 5–30°. For the larger ZIF-8 crystals, 150 mg of zinc nitrate hexahydrate and 115 mg of 2-methylimidazole were used for the synthesis. The two as-synthesized ZIF-8 crystals were characterized using scanning electron microscope (FEI Nova 2300 field-emission SEM at an acceleration voltage of 10 kV). Dynamic light scattering characterization of the two types of synthesized ZIF-8 crystals suspended in cell culture medium was performed using a Malvern Zetasizer Nano ZS system.

VSMC isolation and culture

Male Sprague-Dawley rats used in this study were in accordance with the NIH guidelines (8th Edition of the Guide for the Care and Use of Laboratory Animals). The animal use

protocol was approved by the Laboratory Animal Use Committee of the University of South Dakota (#13–09-15–18C). To isolate VSMCs, the rats were euthanized by carbon dioxide (CO_2) asphyxiation. CO_2 was mixed with pre-existing chamber air at a fill rate of approximately 30% of the chamber volume per minute. Then thoracotomy was followed and descending thoracic aorta was excised. VSMCs were enzymatically isolated from the descending thoracic aorta and seeded onto a collagen-I coated 50 mm glass-bottom dish or a 96-well plate. The cells were maintained in DMEM/F-12 supplemented with 10% FBS, 10 mM HEPES, 2 mM L-glutamine, 1 mM sodium pyruvate, 100 U/ml penicillin, and 100 μg/ml streptomycin in a humidified incubator with 5% CO_2 at 37 °C for 24 h before incubation with ZIF-8 nanoparticles. The cells used in the experiments were maintained in primary culture for 2–3 days without passage.

Cytotoxicity assays

The cytotoxicity of ZIF-8 crystals was examined by the MTT and LDH assays. 100 μl cell suspension in the culture medium was added into a 96 well plate with a seeding density of 20,000 cells per well. The plate was incubated at 37°C in 5% CO_2 for 24 h. Then the medium was replaced with freshly prepared growth media containing ZIF-8 crystals at different concentrations of 0, 6.25, 12.5, 25, 50, 75, and 100 μg/ml. For the MTT assay, after 24 h incubation, the medium was removed, and cells were washed by DPBS. 100 μl of 1.2 mM MTT medium solution was then added to each well. After 4 h, the MTT medium was removed and 200 μl DMSO was added to each well. After incubation for 10 min, the absorbance at 570 nm was determined with a plate reader. For the LDH assay, after 24 h incubation, 50 μl medium from each well was transferred to a new 96-well plate, and CyQUANT™ LDH Cytotoxicity Assay Kit (Thermo Fisher Scientific) was used to analyze the LDH in the medium by following the manufacturer's instructions.

Epi-fluorescence and DIC imaging

The cells were seeded onto a collagen-I coated 50 mm glass-bottom dish and cultured in the standard medium for 24 h. Then the medium was replaced with freshly prepared growth media containing ZIF-8 nanoparticles at different concentrations of 0, 12.5 and 25 μg/ml, and the cells were cultured for another 24 h. For epi-fluorescence imaging, ZIF-8 nanoparticles loaded with FITC were used. The imaging was performed at the 6, 12 and 24 h after adding the nanoparticles, using an Olympus IX71 microscope with 100x oil objective and GFP filter. A total of 50 cells per condition were imaged using Micro-manager software by EMCCD camera (Andor Ultra iXon 888) at 1,024×1,024 pixels. The fluorescence intensity of the cells was analyzed by ImageJ-FIJI software using Corrected Total Cell Fluorescence (CCTF) = integrated density - (Total area of selected cell × mean fluorescence of background). For DIC imaging of cell morphology, after 24 h of incubation with 0, 6.25, 12.5 and 25 μg/ml of ZIF-8 nanoparticles, the cells were imaged using an Olympus IX71 microscope equipped with a Nomarski prism and a 20x air objective. The images were acquired by Solis software using Andor iXon ultra 897 EMCCD camera at 512×512 pixels. For DIC imaging of cell contractility in response to Angiotensin II treatment, after 24 h of incubation with 0, 12.5 and 25 μg/ml of ZIF-8 nanoparticles, the medium was replaced with fresh standard medium, and the DIC images were acquired every 3 min after adding the

Angiotensin II (1 μM) into the medium. 40x air objective was used to observe single cell contraction within 15 min.

AFM Imaging of VSMCs

AFM imaging of untreated and treated VSMCs was performed using a BioScope Resolve AFM (Bruker) operated in Peak Force quantitative nanomechanical mapping mode (PF-QNM mode). PF QNM-Live Cell cantilevers (Bruker) with a spring constant (0.06–0.1 N/m), a tip length of 17 μm, a tip radius of 70 nm, and an opening angle of 15° were used. Before imaging cells, the spring constant of the cantilevers were calibrated by the thermal noise method. The tips were oscillated vertically with a 600 nm-1000 nm amplitude and an 800 pN peak force set point by a sinusoidal piezomotion at a frequency of 0.25 kHz. The cell was scanned using a frequency of 0.125 Hz and 256 pixels per line (256 lines). Before the imaging, the media containing 0, 12.5 and 25 μg/ml of ZIF-8 nanoparticles were removed and replaced with CO_2-independent L-15 medium. During the imaging, cells were maintained at 37 °C through a in-built heating stage on the AFM. AFM images and indentation force curves were analyzed using the NanoScope analysis software (v1.9, Bruker). The retract part of the curve was fitted with the Hertz model for spherical tips:

$$F = \frac{4}{3} \frac{E}{\left(1 - v^2\right)} R^{\frac{1}{2}} \cdot \delta^{\frac{3}{2}}$$

where E is the Young's modulus, δ is the indentation depth, v is the Poisson ratio (0.5 was used here), and R is the radius of the tip curvature (70 nm).

Actin staining and dSTORM imaging

Cells were washed with DPBS three times followed by fixation with 4% PFA for 10 min. Then cells were washed with PBS three times to remove PFA residues. Following the fixation, the cells were permeabilized with 0.1% Triton-X 100 for 10 min in a cytoskeletal buffer (10 mM MES pH 6.1, 150 mM NaCl, 5 mM EGTA, 5 mM glucose, and 5 mM $MgCl_2$). Then cells were washed three times with PBS and incubated with sodium borohydride (0.1%) dissolved in PBS for 10 min to reduce the autofluorescence background that occurred during cell fixation, followed by three washes with PBS. Then the cells were incubated with BlockAid buffer for 1 h to avoid any unspecific binding. Then BlockAid buffer was removed and replaced with Alexa Fluor 568 phalloidin (66μM) dissolved in 1 ml of PBS and incubated at 4°C for overnight. Then the actin staining solution was removed and washed with PBS three times. The cells were post-fixed for 5 min using 4% PFA and washed three times. Imaging buffer (100 mM Tris pH 8, 10 mM NaCl, 0.5 mg/ml glucose oxidase, 40 μg/ml catalase, 10% (w/v) glucose, and 1% MEA) was freshly prepared and added to the imaging dish right before dSTORM imaging.

The dSTORM images were collected using an inverted microscope (Olympus IX73) configured for TIRF illumination using a Hamamatsu ORCA-Flash 4.0 V2 CMOS camera. A collimated 561 nm diode-pumped solid-state laser (Spectra-Physics Excelsior), attenuated by neutral density filters (Thorlabs), passing through a 10X Galilean expander (Thorlabs AC508–300-A), was eventually focused onto the back focal plane of an infinity-corrected

objective (Olympus PlanApo 100x/1.45 Oil). A filter set inside the microscope comprised of a multiline dichroic (Semrock Di01-R405/488/561/635) and emission filter (Semrock FF01–593/40). An imaging sequence of 10,000–30,000 frames recorded at 33 Hz was used to reconstruct a high-resolution STORM image. The ImageJ plugin ThunderSTORM was used to reconstruct the dSTORM images.

Intracellular ROS and zinc assays

Intracellular ROS levels were measured using a cellular ROS assay kit from Abcam (ab113851). This assay kit is based on a cell-permeant fluorescent probe, 2',7'-dichlorodihydrofluorescein diacetate (H2DCFDA), a chemically reduced form of fluorescein used as an indicator for reactive oxygen species (ROS) in cells. The cells were seeded at a density of 20,000 per well in a black 96-well plate. After 24 h of culture, the medium was replaced with freshly prepared growth media containing ZIF-8 crystals at different concentrations of 0, 12.5 and 25 μg/ml. After 24 h of incubation, cells were washed and added with H2DCFDA. After 45 min of incubation, the H2DCFDA solution was removed and washed with PBS. Finally, a fluorescence microplate reader at Ex/Em = 485/538 nm in end point mode was used to quantify the ROS levels. Intracellular zinc levels were determined in a similar manner, whereas another cell-permeant fluorescent probe, Zinquin ethyl ester from Sigma, was used to quantify the intracellular zinc levels. A fluorescence microplate reader at Ex/Em = 355/460 nm in end point mode was used to quantify the zinc levels.

Actin polymerization assay

G-actin was diluted to 0.4 mg/ml by G-buffer supplemented with 0.2 mM ATP and 0.5 mM DTT and left to depolymerize any actin oligomers on ice for 1 h. The solution was centrifuged at 14,000 rpm for 15 min at 4°C and the supernatant was transferred to a new tube. Then 1/10 (v/v, volume of P-buffer to volume of G-actin solution) 10X P-buffer was added into the G-actin solution in the new tube. For the zinc treated samples, zinc nitrate hexahydrate was added into the G-actin solution along with the P-buffer to obtain a 2.7-fold increase in the divalent cation concentration of the system. After 1 h incubation at room temperature, the mixture solution was purified using Amicon ultra centrifugal filters (Sigma, cutoff: 100 kDa) by centrifuging the solution at 6,000 rpm for 10 min and washing with distilled water 4 times. For AFM imaging of actin filaments, 5 μl of remaining solution in the filter was transferred on to a $MgCl_2$ pre-treated mica. After waiting for 15 min, the mica was gently rinsed by pure water and dried in air for subsequent AFM imaging. SCANASYST-AIR probe with 2 nm radius (Bruker) was used to image the actin filaments on mica.

Results and Discussion

Synthesis, characterization, and cytotoxicity of ZIF-8 crystals.

Currently, there are two typical sizes of ZIF-8 which are commonly used for drug loading and delivery applications, including 60–80 nm (can be named as ZIF-8 nanoparticles based on the definition of "nanoparticle") and 150–200 nm in diameter.[16, 17, 26, 42, 43] These two types of ZIF-8 crystals were synthesized using a one-pot approach and the size of the

ZIF-8 was adjusted by varying molar ratio of 2-methyl imidazole to zinc ion.[26, 44] Briefly, 2-methyl imidazole dissolved in methanol was added into zinc nitrate methanol solution. After 5 min of vigorous stirring, the reaction solution turned turbid, indicating the formation of ZIF-8 crystals. Then the ZIF-8 crystals were collected and washed three times in methanol by centrifugation. SEM imaging provided a direct comparison for the two synthesized ZIF-8 crystals including the ZIF-8 nanoparticles with average diameter of 60 nm and the larger ZIF-8 crystals with average diameter of 200 nm (Figure S1). After been suspended in standard cell culture medium, dynamic light scattering characterization revealed a slight increase in diameter and good colloidal stability for both ZIF-8 crystals (Figure S2). For the ZIF-8 nanoparticles, TEM imaging also indicated the monodispersed spherical nanoparticles with average diameter of 60 nm (Figure 1A). The powder X-ray diffraction (XRD) pattern of the synthesized nanoparticles displayed all the typical peaks of ZIF-8 crystals (Figure 1B).[45] Subsequently, two of the most-used biochemical assays in the field of nanotoxicology were employed to evaluate the cytotoxicity of ZIF-8 crystals on primary vascular smooth muscle cells (VSMCs) from rat aorta. To our knowledge, VSMCs have not been used for evaluating the cytotoxicity of ZIF-8. A series of concentrations of ZIF-8 nanoparticles were incubated with VSMCs for 24 h and the cell viability was determined using the "gold standard" MTT assay, which measures the mitochondrial function of the cells. This assay is based on enzymatic conversion of the MTT compound to purple-colored formazan crystals by the mitochondrial dehydrogenases of live cells.[46] As shown in Figure 1C, the cell viability was maintained at over 90% for up to 25 μg/ml of ZIF-8 nanoparticles. However, higher concentrations caused significant cell viability decreases to 70%, 60% and 50% for 50, 75, and 100 μg/ml of ZIF-8 nanoparticles, respectively. Furthermore, LDH cytotoxicity assay was applied to evaluate the cell membrane integrity after incubation with ZIF-8 nanoparticles. The LDH, lactate dehydrogenase, is a cytosolic enzyme present in different cell types that is released into the cell culture medium upon damage to the cell membrane. The results (Figure 1D) indicated cell membrane damage at higher concentrations of ZIF-8 nanoparticles (75, and 100 μg/ml). Interestingly, for the larger size ZIF-8 crystals (200 nm in diameter), MTT and LDH assays showed these crystals had less toxicity on VSMCs, compared to 60 nm ZIF-8 nanoparticles, at the same concentrations (Figure S3). We hypothesized this could be because 60 nm was the optimal size for cell uptake, which was demonstrated by other nanoparticles.[47] To test this hypothesis, we conducted an intracellular zinc assay on VSMCs after incubation with 25 μg/ml of 60 nm and 200 nm ZIF-8 crystals for 24 h (Figure S4). The results showed that 200 nm ZIF-8 crystals only caused 1.6-fold increase in the intracellular Zn^{2+} concentration, whereas 60 nm ZIF-8 nanoparticles led to 2.7-fold increase, suggesting higher uptake of 60 nm ZIF-8 nanoparticles by the VSMCs. Therefore, we focused on the more cytotoxic 60 nm ZIF-8 nanoparticles in the subsequent studies. According to MTT and LDH assays, we could define a "safe dose" threshold for the ZIF-8 nanoparticles on VSMCs, which should be around 25 μg/ml. We selected the two "safe doses", 12.5 and 25 μg/ml, to investigate the effects of ZIF-8 nanoparticles on VSMCs.

ZIF-8 nanoparticle uptake by VSMCs and effect on cell morphology.

The cell uptake of ZIF-8 nanoparticles by VSMCs was validated by fluorescence microscopy. The ZIF-8 nanoparticles were loaded with a fluorescence dye, fluorescein

isothiocyanate (FITC), during the one-pot synthesis, to facilitate the fluorescence imaging of ZIF-8 nanoparticles in the cells. A previous study has shown that negatively charged small molecules such as fluorescein had a tendency to be encapsulated into the ZIF-8 framework during the nanoparticle formation.[26] The fluorescence images and quantitative analysis based on correlated total cell fluorescence (CTCF) indicated the uptake of ZIF-8 nanoparticles by VMSCs in a time and concentration dependent manner (Figure 2A–2D, and S5–S6). With increased incubation time and nanoparticle concentrations, the VSMCs showed increased fluorescence intensity, indicating the increased uptake of ZIF-8 nanoparticles by VSMCs. The nanoparticles appeared to be uniformly distributed throughout the cells. Interestingly, especially for the 12.5 μg/ml concentration (Figure 2A), some bright spots could be observed in the cells, suggesting the endocytosis of the ZIF-8 nanoparticles, where several ZIF-8 nanoparticles were engulfed within single endosomes.[48] As a negative control, the VSMCs were incubated with pure ZIF-8 nanoparticles and the cells did not show any fluorescence (Figure S6). Apart from the increased fluorescence intensity, it should be noted that the fluorescence profiles of the cells also appeared to change with the increase of incubation time and nanoparticle concentrations (Figure 2A and 2C). This inspired us to investigate the effect of ZIF-8 nanoparticles on the morphology of VSMCs under these "safe" concentrations. Differential interference contrast (DIC) microscopy was used to image the cells with better contrast, allowing for precise quantification of cell morphology. Figure 2E shows the DIC images of VSMCs after 24 h incubation with standard cell culture medium (control) and cell culture media containing 12.5 and 25 μg/ml of ZIF-8 nanoparticles. After culturing in standard medium for 24 h, VSMCs manifested an elongated shape, the typical morphology of primary VSMCs. It is well known that VSMCs in native blood vessel walls have an elongated morphology and are aligned in the circumferential direction with a well-organized structure.[49] However, after incubation with 12.5 and 25 μg/ml of ZIF-8 nanoparticles for 24 h, the cells exhibited a less elongated, and more spread shape. Here, we used the aspect ratio (i.e., long axis to short axis) to quantify the cell morphology change after incubation with ZIF-8 nanoparticles. The results showed that the VSMCs became less elongated and more spread (i.e., lower aspect ratios), with the increase of ZIF-8 nanoparticle concentration (Figure 2F). We also found that the aspect ratio of VSMCs decreased progressively with the increase of incubation time with 25 μg/ml of ZIF-8 nanoparticles (0 h, 6 h, 12 h and 24 h, Figure S7). Interestingly, at a lower concentration (6.25 μg/ml, Figure S8), the VSMCs had almost identical morphology and aspect ratio as the control cells, suggesting that 12.5 ug/ml is the minimum toxic concentration from the cell morphology perspective. These results led to important questions: Is the "safe dose" determined by the biochemical cell assays really safe? And is the morphology change of VSMCs seen here a safety concern for the use of ZIF-8 based therapeutics?

Effect of ZIF-8 nanoparticles on VSMC contractility.

The relationship between structure and function is widely recognized as a central concept in cell biology.[50, 51] Since we observed low doses of ZIF-8 nanoparticles led to morphological changes in VSMCs, we further investigated how the function of VSMCs was affected. The main function of VSMCs is to maintain the tone of blood vessels and to control the blood flow through the contraction of the cells. Thus, the elongated cell shape is

also named as the "contractile phenotype", implying the excellent contractility of the VSMCs.[52] Herein, a classic vasoconstrictor (Angiotensin II) was used to study the contractility of VSMCs. Angiotensin II is a crucial hormone in the regulation of plasma volume, vasoconstriction, and blood pressure, as it activates the contraction of VSMCs.[53, 54] Time-lapse DIC imaging was applied to observe the contraction of single VSMCs in response to Angiotensin II. As expected, for the control VSMCs (non-treated), within 15 min after adding Angiotensin II, the cells became shorter with increasing time, leading to significantly decreased aspect ratio, from 12 to 4 (Figure 3A, 3D, and S9). The decreased aspect ratio here is a quantitative indicator for VSMC contractility. In stark contrast, the VSMCs after incubation with ZIF-8 nanoparticles showed no response to Angiotensin II treatments, as indicated by the unchanged aspect ratios (Figure 3B–3C, 3E–3F, and S10–S11). These results indicate that the VSMC morphology and contractility were both altered by the ZIF-8 nanoparticles, even though the concentrations (12.5 and 25 μg/ml) were deemed "safe" by biochemical cell assays. It was found that the altered VSMC morphology and contractility cannot be recovered by switching back to the normal cell medium for 72 h extended culturing (Figure S12). In addition to the cell contractility, a wound healing assay (i.e., "scratch assay") was performed to quantify the migration ability of VSMCs with and without ZIF-8 treatment. As shown in Figure S13, without any treatment, the cells did not migrate within 24 h, leading to 0% wound healing. In contrast, the cell after being treated with 25 μg/ml ZIF-8 nanoparticles showed moderate migration, corresponding to ~25% wound healing (Figure S14). Based on the fact that the non-contractile conversion of VSMC phenotype, loss of contractility, and migration toward the intima of the blood vessel are fundamental to the development of atherosclerosis and related cardiovascular diseases,[55] we believe low doses of ZIF-8 nanoparticles could still be a safety concern in terms of cardiovascular risks.

AFM and dSTORM investigation of VSMC actin organization at single cell level.

To understand how the VSMC morphology and contractility were altered by the ZIF-8 nanoparticles, we turned our attention to the actin organization of VSMCs, considering actin filaments (filamentous actin, F-actin) are the key structures that control the contraction of the VSMCs.[56, 57]

Atomic force microscopy (AFM) is a unique tool for high resolution imaging of cell morphology and quantitative characterization of cell mechanics under physiological conditions.[58] In this study, we employed a fast force imaging mode of AFM, namely, Peak-Force quantitative nanomechanical mapping. Unlike conventional force-volume mode in which the indentation force curves are collected by linearly ramping the tip at each pixel, the Peak-Force mapping oscillates the tip vertically with a large amplitude (e.g., 600 nm) by a sinusoidal piezomotion at the frequency of 0.1–2 kilohertz (versus 0.1–1 Hz in the conventional force-volume mode).[59–61] Therefore, the Peak-Force mode can map the Young's modulus of the entire living cell surface with the same lateral resolution as that of simultaneous topography imaging (image pixel: 256×256) in a short period of time (<30 min), which is extremely valuable to correlate cell surface topography with stiffness. For example, a previous study has applied this technique to visualize the actin organization at the apical surfaces of living cancer cells using stiffness images since apical F-actin provides a

dominant contribution to cell stiffness (Figure 4A).[62] As shown in Figure 4, the height, peak force error (displaying details of cell surface topography), and Young's modulus maps of single VSMCs were acquired simultaneously. The value of each pixel in the Young's modulus map was obtained by fitting the indentation force curve using the Hertz model based on a spherical AFM tip Figure 4B–4C, and S15). For the untreated VSMCs (control), the cells displayed an elongated shape with grooved surface topography (Figure 4D and S16). Notably, the Young's modulus map also manifested this "grooved" pattern showing perfect correlation with the height and peak force error maps. The high modulus regions always correlated with the higher areas on the cell surfaces, owing to the stiffer actin filaments underneath the plasma membrane. These well-aligned actin filaments, parallel to the long axes of the cells, are critical to generate contractile forces for VSMCs. For the VSMCs incubated with culture medium containing 12.5 μg/ml ZIF-8 nanoparticles, the cells started to show a spread morphology, consistent with DIC images. The long axes of the cells were still recognizable with parallel actin filaments, whereas some actin filaments not parallel to the long axes also developed concomitant with the spreading of the cells (Figure 4E, and S17). For the VSMCs incubated with culture medium containing 25 μg/ml ZIF-8 nanoparticles, a more spread cell morphology was present, and it became difficult to identify the long axes of the cells. Remarkably, actin branches and networks can be observed (Figure 4F, and S18), as opposed to the well aligned parallel filaments observed in control cells. Overall, the AFM imaging shows that ZIF-8 nanoparticles altered the VSMC morphology and actin organization in a concentration-dependent manner.

To further confirm the altered actin organization of VSMCs by ZIF-8 nanoparticles, we employed a super-resolution fluorescence imaging approach, direct stochastic optical reconstruction microscopy (dSTORM), to visualize the detailed actin cytoskeleton structures at the basal layers of the cells. The use of total internal reflection fluorescence (TIRF) microscopy mode in dSTORM limits the fluorophore excitation to a thin evanescent field (100–200 nm), and the background signal from out-of-focus planes are all eliminated, thereby only F-actin at the basal layers of cells are imaged (Figure 5A). Compared to a conventional fluorescence microscope, dSTORM achieves sub-diffraction limited resolution fluorescence imaging by a unique mechanism: chemical manipulation of fluorophores to make them photo-switchable in a stochastic manner, followed by image processing to localize the single fluorescent emitters at nanometer precision (Figure 5B).[63–65] As shown in Figure 5C–5E, dSTORM offers a spatial resolution superior to that of conventional fluorescence microscopy to resolve the detailed actin cytoskeleton structures at the basal layers of VSMCs. For the untreated cells (control, Figure 5C and S19), well-aligned actin filaments parallel to the long axes of the cells were present, indicating the VSMCs also possessed these contractile filaments at the basal layers. However, for the ZIF-8 treated cells, the actin organization at the basal layers was drastically altered (Figure 5D–5E, S20–S21), especially for the cells treated by 25 μg/ml ZIF-8 nanoparticles. The dSTORM images clearly displayed the formation of actin branches and networks at the basal layers of the cells (Figure 5E and S21). Taken together, the AFM and dSTORM imaging demonstrates that the used low doses of ZIF-8 nanoparticles altered the actin organization of entire VSMCs including both apical and basal surfaces. This disruption of the actin cytoskeleton and the resulting altered cell morphology are the causes of the observed loss of cell contractility.

Actin polymerization assay studying the effect of Zn^{2+} on actin assembly.

In the light of our AFM and dSTORM findings, we investigated the potential mechanism for ZIF-8 nanoparticles' disruption of the actin organization in VSMCs. Previous literature suggested two possible factors could account for the altered actin cytoskeleton by metal-based nanoparticles: (i) Studies have found that exposure of cells to metal-based nanoparticles such as gold nanoparticles is accompanied by an increased level of reactive oxygen species (ROS), a pivotal modulator of actin organization, because cytoskeletal proteins including actin are sensitive to ROS oxidative stress;[24, 66, 67] and (ii) Released metal ions as a result of nanoparticle dissociation in the cells drastically increases the concentration of intracellular metal ions, either directly affecting the actin assembly process or by increasing the ROS level to alter the actin organization.[68–72] To elucidate the possible mechanism, we first examined the intracellular ROS levels of VSMCs after incubation with ZIF-8 nanoparticles for 24 h (Figure S22). At both concentrations (12.5 and 25 μg/ml), we did not see obvious increase in ROS levels in the cells, compared to untreated cells. This is not surprising since elevated ROS levels are typically associated with malfunctioned mitochondria and we did not see significant cell viability decrease (in the MTT assay) under these two concentrations. Next, we measured the intracellular Zn^{2+} levels of VSMCs after incubation with ZIF-8 nanoparticles for 24 h (Figure S22). Interestingly, compared to untreated cells, the intracellular Zn^{2+} levels had a 1.8- and 2.7-fold increase for cells treated with 12.5 and 25 μg/ml ZIF-8 nanoparticles, respectively. Normally, cells require small amounts of Zn^{2+} for distinct intracellular processes so there are tightly controlled and saturable mechanisms in the cell membrane that maintain the cytoplasmic zinc homeostasis. However, these precise mechanisms can be bypassed when ZIF-8 nanoparticles are endocytosed by the cell.[68] Considering that ZIF-8 nanoparticles are not stable in acidic environments as the coordination bonds between Zn^{2+} and organic ligand can be broken by the acidic pH, the increased intracellular Zn^{2+} could be because the ZIF-8 nanoparticles engulfed in the cells were dissolved in the acidic endosomes and/or lysosomes (pH=4–6), releasing the free Zn^{2+} to cytoplasm.[17, 26] To confirm the increased intracellular Zn^{2+} was indeed from ZIF-8 nanoparticles internalized by the cells, we conducted a control experiment using ZIF-8 nanoparticle "conditioned" culture medium: The 25 μg/ml ZIF-8 nanoparticles were incubated with standard cell culture medium for 24 h, subjected to centrifugation, and supernatant was collected and used to culture VSMCs for another 24 h. The results indicated that intracellular Zn^{2+}, ROS, cell morphology, and actin organization of these cells remained unchanged, similar to untreated cells (Figure S22 and S23). According to the recent published stability of ZIF-8 in the standard cell medium, ~10% of ZIF-8 can be degraded by the cell culture medium within 24 h.[73] Then we can estimate the dissolved Zn^{2+} and 2-methyl imidazole amount in the cell medium. Therefore, another two control experiments were performed using a cell culture medium with 0.72 μg/ml of Zn^{2+} (by adding zinc nitrate into the medium) and a cell culture medium with 1.78 μg/ml of 2-methyl imidazole, respectively, assuming 10% of ZIF-8 were degraded by the cell medium. The AFM imaging showed similar results as the first control experiments did, where the cell morphology and actin organization remained unaffected (Figure S24 and S25). These experiments suggest the internalized ZIF-8 nanoparticles, not Zn^{2+} released extracellularly, caused the increase of intracellular Zn^{2+}, which differs from previous studies showing that ZIF-8 microparticles released Zn^{2+} in the medium and caused the cytotoxicity.

[27, 73] Moreover, the impact of the organic ligand (i.e., 2-methyl imidazole) on VSMCs can be neglected. Overall, these experiments demonstrate that, under these ZIF-8 nanoparticle concentrations, increased intracellular Zn^{2+} due to the dissociation of internalized ZIF-8 nanoparticles did not increase the intracellular ROS levels, and thereby the altered actin organization was not related to intracellular ROS levels. Therefore, the change of actin organization could be due to the direct impact of intracellular zinc increase. Certainly, with the further increase of ZIF-8 nanoparticle concentrations, the intracellular zinc could keep increasing, causing the ROS production and further change of the actin cytoskeleton (which will be an indirect impact).

Therefore, we hypothesized that the increased intracellular Zn^{2+} directly affected the actin organization, considering that actin monomer (globular or G-actin) contains several Zn^{2+} binding sites, and the highly dynamic actin assembly/disassembly process in the cells (G-actin ↔ actin filament, single actin filament ↔ actin bundles) can be affected by several divalent cations.[74, 75] To test this hypothesis, we performed a well-established actin polymerization assay to understand how increased Zn^{2+} affected the actin organization. This assay, including G-actin, ATP, and divalent cation in a buffering system, is a simplified model to mimic the actin assembly process within the cells.[76–78] Here, the normal assay condition represented actin assembly process in the untreated VSMCs, whereas this process in the ZIF-8 nanoparticle treated cells was simulated through increasing the divalent cation concentration in the assay by adding Zn^{2+} until a 2.7-fold of increase in divalent cation concentration (as measured in the cells) was reached. Then the actin filaments were collected and characterized by AFM imaging. For the assay performed under normal conditions, single actin filaments assembled from actin monomers can be clearly observed, with a structure similar to a string of beads (Figure 6A and 6D). In the normal VSMCs, these single actin filaments are fundamental structures that will further assemble to bundles with actin-binding proteins to drive the cell contraction (Figure 7, left column). In contrast, the assay performed with increased Zn^{2+} generated completely different actin structures. Instead of forming single, linear filaments from actin monomers, the actin filaments showed bundles, branches, and networks during the polymerization process (Figure 6B–6C, 6E–6F, and S26). Interestingly, the network structures were similar to what we observed from AFM and dSTROM images, in which several actin bundles pointing to diverse directions were originated from a common site, indicating the formation of branched networks. We suggest that the actin bundles and networks already formed during the actin polymerization process, due to the increased intracellular Zn^{2+}, may block the binding sites on single filaments for actin-binding proteins such as myosin-II and thereby hinder the formation of actomyosin bundles, which drives the contraction of VSMCs (Figure 7, right column). In summary, the actin polymerization assay here provides a simplified model to elucidate the effect of internalized ZIF-8 nanoparticles on the cell actin organization. As illustrated in Figure 7, under normal conditions (untreated cells), G-actin assembles to single actin filaments, and subsequently the single filaments interact with actin-binding proteins such as myosin-II to form well-aligned actomyosin bundles, driving the contraction of cells. Upon uptake of ZIF-8 nanoparticles, ZIF-8 nanoparticles dissolve in acidic endosomes/lysosomes and release Zn^{2+} into the cytoplasm, leading to increased intracellular Zn^{2+} levels. With increased intracellular Zn^{2+}, the G-actin assembles to actin bundles and networks, instead of

linear, single actin filaments, during the actin polymerization process. Essentially, the actin cytoskeleton remodeling process is likely impacted by the increased intracellular Zn^{2+} levels, thus hindering the formation of well-aligned contractile filaments (i.e., actomyosin bundles) and the contraction of VSMCs.

Conclusion

We have investigated the effects of conventionally low doses of ZIF-8 nanoparticles on VSMC morphology, actin organization, and contractility. Instead of relying on conventional cytotoxicity assays, which only provide end-point results through biochemical reactions, we focused on the biophysical changes of VSMCs induced by the ZIF-8 nanoparticles at the single cell level. By using two nanoscale imaging tools, AFM and dSTORM, we found that, even at the concentrations that were determined to be "safe" by biochemical cell assays, ZIF-8 nanoparticles still caused changes in cell morphology and actin cytoskeleton organization at the cell apical and basal surfaces. These biophysical structural changes further impaired the contractility function of VSMCs in response to Angiotensin II, a classic vasoconstrictor. Based on an actin polymerization assay, we concluded that the increased intracellular Zn^{2+} concentration due to the uptake and dissociation of ZIF-8 nanoparticles could cause the actin cytoskeleton dis-organization, as the elevated Zn^{2+} directly disrupted the actin assembly process in our actin polymerization assay, leading to altered actin organization such as branches and networks. Since the VSMC phenotype change and loss of contractility are fundamental to the development of atherosclerosis and related cardiovascular diseases, we believe these low doses of ZIF-8 nanoparticles administered intravenously could still be a safety concern in terms of cardiovascular risks. Moving forward, it is imperative to re-consider the "safe" nanoparticle doses that are determined by biochemical cell assays alone, and take into account the impact of these nanoparticles on biophysical characteristics of cells including the actin cytoskeleton and cell morphology, especially in the case of intravenously administered MOF and other metal-based nanomaterials on vascular smooth muscle cells. More broadly, the biophysical characteristics of vascular smooth muscle cells can serve as an important indicator to evaluate the toxicity of nanomaterials.

Supplementary Material

Refer to Web version on PubMed Central for supplementary material.

Acknowledgements

References

[1]. Liu Y, Zhao Y, Chen X, Bioengineering of Metal-organic Frameworks for Nanomedicine, Theranostics, 9 (2019) 3122–3133. [PubMed: 31244945]

[2]. Wu M-X, Yang Y-W, Metal–Organic Framework (MOF)-Based Drug/Cargo Delivery and Cancer Therapy, Advanced Materials, 29 (2017) 1606134.

[3]. Wang Y, Yan J, Wen N, Xiong H, Cai S, He Q, Hu Y, Peng D, Liu Z, Liu Y, Metal-organic frameworks for stimuli-responsive drug delivery, Biomaterials, 230 (2020) 119619. [PubMed: 31757529]

[4]. Lu K, Aung T, Guo N, Weichselbaum R, Lin W, Nanoscale Metal–Organic Frameworks for Therapeutic, Imaging, and Sensing Applications, Advanced Materials, 30 (2018) 1707634.

[5]. Zhang W, Lu J, Gao X, Li P, Zhang W, Ma Y, Wang H, Tang B, Enhanced Photodynamic Therapy by Reduced Levels of Intracellular Glutathione Obtained By Employing a Nano-MOF with CuII as the Active Center, Angewandte Chemie International Edition, 57 (2018) 4891–4896. [PubMed: 29451722]

[6]. Wan X, Song L, Pan W, Zhong H, Li N, Tang B, Tumor-Targeted Cascade Nanoreactor Based on Metal–Organic Frameworks for Synergistic Ferroptosis–Starvation Anticancer Therapy, ACS Nano, 14 (2020) 11017–11028. [PubMed: 32786253]

[7]. Wang C, Tadepalli S, Luan J, Liu K-K, Morrissey JJ, Kharasch ED, Naik RR, Singamaneni S, Metal-Organic Framework as a Protective Coating for Biodiagnostic Chips, Advanced Materials, 29 (2017) 1604433.

[8]. Tadepalli S, Yim J, Cao S, Wang Z, Naik RR, Singamaneni S, Metal–Organic Framework Encapsulation for the Preservation and Photothermal Enhancement of Enzyme Activity, Small, 14 (2018) 1702382.

[9]. Liang K, Ricco R, Doherty CM, Styles MJ, Bell S, Kirby N, Mudie S, Haylock D, Hill AJ, Doonan CJ, Falcaro P, Biomimetic mineralization of metal-organic frameworks as protective coatings for biomacromolecules, Nature Communications, 6 (2015) 7240.

[10]. Luzuriaga MA, Welch RP, Dharmarwardana M, Benjamin CE, Li S, Shahrivarkevishahi A, Popal S, Tuong LH, Creswell CT, Gassensmith JJ, Enhanced Stability and Controlled Delivery of MOF-Encapsulated Vaccines and Their Immunogenic Response In Vivo, ACS Applied Materials & Interfaces, 11 (2019) 9740–9746. [PubMed: 30776885]

[11]. Wang C, Sun H, Luan J, Jiang Q, Tadepalli S, Morrissey JJ, Kharasch ED, Singamaneni S, Metal–Organic Framework Encapsulation for Biospecimen Preservation, Chemistry of Materials, 30 (2018) 1291–1300.

[12]. Feng Y, Wang H, Zhang S, Zhao Y, Gao J, Zheng Y, Zhao P, Zhang Z, Zaworotko MJ, Cheng P, Ma S, Chen Y, Antibodies@MOFs: An In Vitro Protective Coating for Preparation and Storage of Biopharmaceuticals, Advanced Materials, 31 (2019) 1805148.

[13]. Doonan C, Riccò R, Liang K, Bradshaw D, Falcaro P, Metal–Organic Frameworks at the Biointerface: Synthetic Strategies and Applications, Accounts of Chemical Research, 50 (2017) 1423–1432. [PubMed: 28489346]

[14]. Sun H, Li Y, Yu S, Liu J, Metal-organic frameworks (MOFs) for biopreservation: From biomacromolecules, living organisms to biological devices, Nano Today, 35 (2020) 100985.

[15]. Welch RP, Lee H, Luzuriaga MA, Brohlin OR, Gassensmith JJ, Protein–Polymer Delivery: Chemistry from the Cold Chain to the Clinic, Bioconjugate Chemistry, 29 (2018) 2867–2883. [PubMed: 30152998]

[16]. Chen T-T, Yi J-T, Zhao Y-Y, Chu X, Biomineralized Metal–Organic Framework Nanoparticles Enable Intracellular Delivery and Endo-Lysosomal Release of Native Active Proteins, Journal of the American Chemical Society, 140 (2018) 9912–9920. [PubMed: 30008215]

[17]. Zheng H, Zhang Y, Liu L, Wan W, Guo P, Nyström AM, Zou X, One-pot Synthesis of Metal–Organic Frameworks with Encapsulated Target Molecules and Their Applications for Controlled Drug Delivery, Journal of the American Chemical Society, 138 (2016) 962–968. [PubMed: 26710234]

[18]. Zhang L, Wang Z, Zhang Y, Cao F, Dong K, Ren J, Qu X, Erythrocyte Membrane Cloaked Metal–Organic Framework Nanoparticle as Biomimetic Nanoreactor for Starvation-Activated Colon Cancer Therapy, ACS Nano, 12 (2018) 10201–10211. [PubMed: 30265804]

[19]. Chen W-H, Luo G-F, Vázquez-González M, Cazelles R, Sohn YS, Nechushtai R, Mandel Y, Willner I, Glucose-Responsive Metal–Organic-Framework Nanoparticles Act as "Smart" Sense-and-Treat Carriers, ACS Nano, 12 (2018) 7538–7545. [PubMed: 29969227]

[20]. Wang C, Sudlow G, Wang Z, Cao S, Jiang Q, Neiner A, Morrissey JJ, Kharasch ED, Achilefu S, Singamaneni S, Metal-Organic Framework Encapsulation Preserves the Bioactivity of Protein Therapeutics, Advanced Healthcare Materials, 7 (2018) 1800950.

[21]. Li Y, Zhang K, Liu P, Chen M, Zhong Y, Ye Q, Wei MQ, Zhao H, Tang Z, Encapsulation of Plasmid DNA by Nanoscale Metal–Organic Frameworks for Efficient Gene Transportation and Expression, Advanced Materials, 31 (2019) 1901570.

[22]. Alsaiari SK, Patil S, Alyami M, Alamoudi KO, Aleisa FA, Merzaban JS, Li M, Khashab NM, Endosomal Escape and Delivery of CRISPR/Cas9 Genome Editing Machinery Enabled by Nanoscale Zeolitic Imidazolate Framework, Journal of the American Chemical Society, 140 (2018) 143–146. [PubMed: 29272114]

[23]. Tamames-Tabar C, Cunha D, Imbuluzqueta E, Ragon F, Serre C, Blanco-Prieto MJ, Horcajada P, Cytotoxicity of nanoscaled metal–organic frameworks, Journal of Materials Chemistry B, 2 (2014) 262–271. [PubMed: 32261505]

[24]. Ma X, Hartmann R, Jimenez de Aberasturi D, Yang F, Soenen SJH, Manshian BB, Franz J, Valdeperez D, Pelaz B, Feliu N, Hampp N, Riethmüller C, Vieker H, Frese N, Gölzhäuser A, Simonich M, Tanguay RL, Liang X-J, Parak WJ, Colloidal Gold Nanoparticles Induce Changes in Cellular and Subcellular Morphology, ACS Nano, 11 (2017) 7807–7820. [PubMed: 28640995]

[25]. Setyawati MI, Sevencan C, Bay BH, Xie J, Zhang Y, Demokritou P, Leong DT, Nano-TiO2 Drives Epithelial–Mesenchymal Transition in Intestinal Epithelial Cancer Cells, Small, 14 (2018) 1800922.

[26]. Zhuang J, Kuo C-H, Chou L-Y, Liu D-Y, Weerapana E, Tsung C-K, Optimized Metal–Organic-Framework Nanospheres for Drug Delivery: Evaluation of Small-Molecule Encapsulation, ACS Nano, 8 (2014) 2812–2819. [PubMed: 24506773]

[27]. Hoop M, Walde CF, Riccò R, Mushtaq F, Terzopoulou A, Chen X-Z, deMello AJ, Doonan CJ, Falcaro P, Nelson BJ, Puigmartí-Luis J, Pané S, Biocompatibility characteristics of the metal organic framework ZIF-8 for therapeutical applications, Applied Materials Today, 11 (2018) 13–21.

[28]. Setyawati MI, Tay CY, Bay BH, Leong DT, Gold Nanoparticles Induced Endothelial Leakiness Depends on Particle Size and Endothelial Cell Origin, ACS Nano, 11 (2017) 5020–5030. [PubMed: 28422481]

[29]. Setyawati MI, Tay CY, Chia SL, Goh SL, Fang W, Neo MJ, Chong HC, Tan SM, Loo SCJ, Ng KW, Xie JP, Ong CN, Tan NS, Leong DT, Titanium dioxide nanomaterials cause endothelial cell leakiness by disrupting the homophilic interaction of VE–cadherin, Nature Communications, 4 (2013) 1673.

[30]. Napierska D, Thomassen LCJ, Rabolli V, Lison D, Gonzalez L, Kirsch-Volders M, Martens JA, Hoet PH, Size-Dependent Cytotoxicity of Monodisperse Silica Nanoparticles in Human Endothelial Cells, Small, 5 (2009) 846–853. [PubMed: 19288475]

[31]. Cao Y, Gong Y, Liu L, Zhou Y, Fang X, Zhang C, Li Y, Li J, The use of human umbilical vein endothelial cells (HUVECs) as an in vitro model to assess the toxicity of nanoparticles to endothelium: a review, Journal of Applied Toxicology, 37 (2017) 1359–1369. [PubMed: 28383141]

[32]. Hadi HAR, Carr CS, Al Suwaidi J, Endothelial dysfunction: cardiovascular risk factors, therapy, and outcome, Vasc Health Risk Manag, 1 (2005) 183–198. [PubMed: 17319104]

[33]. Rajendran P, Rengarajan T, Thangavel J, Nishigaki Y, Sakthisekaran D, Sethi G, Nishigaki I, The vascular endothelium and human diseases, International journal of biological sciences, 9 (2013) 1057. [PubMed: 24250251]

[34]. Komarova Y, Malik AB, Regulation of endothelial permeability via paracellular and transcellular transport pathways, Annual review of physiology, 72 (2010) 463–493.

[35]. Wang K-C, Yeh Y-T, Nguyen P, Limqueco E, Lopez J, Thorossian S, Guan K-L, Li Y-SJ, Chien S, Flow-dependent YAP/TAZ activities regulate endothelial phenotypes and atherosclerosis, Proceedings of the National Academy of Sciences, 113 (2016) 11525.

[36]. Tee JK, Yip LX, Tan ES, Santitewagun S, Prasath A, Ke PC, Ho HK, Leong DT, Nanoparticles' interactions with vasculature in diseases, Chemical Society Reviews, 48 (2019) 5381–5407. [PubMed: 31495856]

[37]. Bennett MR, Sinha S, Owens GK, Vascular Smooth Muscle Cells in Atherosclerosis, Circ Res, 118 (2016) 692–702. [PubMed: 26892967]

[38]. Doran AC, Meller N, McNamara CA, Role of smooth muscle cells in the initiation and early progression of atherosclerosis, Arteriosclerosis, thrombosis, and vascular biology, 28 (2008) 812–819.

[39]. Ren J, Zhou T, Pilli VSS, Phan N, Wang Q, Gupta K, Liu Z, Sheibani N, Liu B, Novel Paracrine Functions of Smooth Muscle Cells in Supporting Endothelial Regeneration Following Arterial Injury, Circ Res, 124 (2019) 1253–1265. [PubMed: 30739581]

[40]. Hong Z, Sun Z, Li M, Li Z, Bunyak F, Ersoy I, Trzeciakowski JP, Staiculescu MC, Jin M, Martinez-Lemus L, Hill MA, Palaniappan K, Meininger GA, Vasoactive agonists exert dynamic and coordinated effects on vascular smooth muscle cell elasticity, cytoskeletal remodelling and adhesion, The Journal of physiology, 592 (2014) 1249–1266. [PubMed: 24445320]

[41]. Sanyour HJ, Li N, Rickel AP, Childs JD, Kinser CN, Hong Z, Membrane cholesterol and substrate stiffness co-ordinate to induce the remodelling of the cytoskeleton and the alteration in the biomechanics of vascular smooth muscle cells, Cardiovascular Research, 115 (2018) 1369–1380.

[42]. Tiwari A, Singh A, Garg N, Randhawa JK, Curcumin encapsulated zeolitic imidazolate frameworks as stimuli responsive drug delivery system and their interaction with biomimetic environment, Scientific Reports, 7 (2017) 12598. [PubMed: 28974697]

[43]. Jiang Z, Wang Y, Sun L, Yuan B, Tian Y, Xiang L, Li Y, Li Y, Li J, Wu A, Dual ATP and pH responsive ZIF-90 nanosystem with favorable biocompatibility and facile post-modification improves therapeutic outcomes of triple negative breast cancer in vivo, Biomaterials, 197 (2019) 41–50. [PubMed: 30640136]

[44]. Bux H, Liang F, Li Y, Cravillon J, Wiebcke M, Caro J, Zeolitic Imidazolate Framework Membrane with Molecular Sieving Properties by Microwave-Assisted Solvothermal Synthesis, Journal of the American Chemical Society, 131 (2009) 16000–16001. [PubMed: 19842668]

[45]. Park KS, Ni Z, Côté AP, Choi JY, Huang R, Uribe-Romo FJ, Chae HK, O'Keeffe M, Yaghi OM, Exceptional chemical and thermal stability of zeolitic imidazolate frameworks, Proceedings of the National Academy of Sciences, 103 (2006) 10186–10191.

[46]. Sha B, Gao W, Wang S, Xu F, Lu T, Cytotoxicity of titanium dioxide nanoparticles differs in four liver cells from human and rat, Composites Part B: Engineering, 42 (2011) 2136–2144.

[47]. Chithrani BD, Ghazani AA, Chan WCW, Determining the Size and Shape Dependence of Gold Nanoparticle Uptake into Mammalian Cells, Nano Letters, 6 (2006) 662–668. [PubMed: 16608261]

[48]. Hayakawa A, Leonard D, Murphy S, Hayes S, Soto M, Fogarty K, Standley C, Bellve K, Lambright D, Mello C, Corvera S, The WD40 and FYVE domain containing protein 2 defines a class of early endosomes necessary for endocytosis, Proceedings of the National Academy of Sciences, 103 (2006) 11928–11933.

[49]. Chang S, Song S, Lee J, Yoon J, Park J, Choi S, Park JK, Choi K, Choi C, Phenotypic modulation of primary vascular smooth muscle cells by short-term culture on micropatterned substrate, PloS one, 9 (2014) e88089. [PubMed: 24505388]

[50]. Liu H, Wu M, Jia Y, Niu L, Huang G, Xu F, Control of fibroblast shape in sequentially formed 3D hybrid hydrogels regulates cellular responses to microenvironmental cues, NPG Asia Materials, 12 (2020) 45.

[51]. Wang M, Yang Y, Han L, Xu F, Li F, Cell mechanical microenvironment for cell volume regulation, Journal of Cellular Physiology, 235 (2020) 4070–4081. [PubMed: 31637722]

[52]. Worth NF, Rolfe BE, Song J, Campbell GR, Vascular smooth muscle cell phenotypic modulation in culture is associated with reorganisation of contractile and cytoskeletal proteins, Cell Motility, 49 (2001) 130–145.

[53]. Wynne BM, Chiao C-W, Webb RC, Vascular Smooth Muscle Cell Signaling Mechanisms for Contraction to Angiotensin II and Endothelin-1, J Am Soc Hypertens, 3 (2009) 84–95. [PubMed: 20161229]

[54]. Do KH, Kim MS, Kim JH, Rhim B-Y, Lee WS, Kim CD, Bae SS, Angiotensin II-induced aortic ring constriction is mediated by phosphatidylinositol 3-kinase/L-type calcium channel signaling pathway, Experimental & Molecular Medicine, 41 (2009) 569–576. [PubMed: 19381068]

[55]. Basatemur GL, Jørgensen HF, Clarke MCH, Bennett MR, Mallat Z, Vascular smooth muscle cells in atherosclerosis, Nature Reviews Cardiology, 16 (2019) 727–744. [PubMed: 31243391]

[56]. Seawright JW, Sreenivasappa H, Gibbs HC, Padgham S, Shin SY, Chaponnier C, Yeh AT, Trzeciakowski JP, Woodman CR, Trache A, Vascular Smooth Muscle Contractile Function Declines With Age in Skeletal Muscle Feed Arteries, Frontiers in Physiology, 9 (2018).

[57]. Gunst SJ, Zhang W, Actin cytoskeletal dynamics in smooth muscle: a new paradigm for the regulation of smooth muscle contraction, American journal of physiology. Cell physiology, 295 (2008) C576–587. [PubMed: 18596210]

[58]. Wang C, Yadavalli VK, Investigating biomolecular recognition at the cell surface using atomic force microscopy, Micron, 60 (2014) 5–17. [PubMed: 24602267]

[59]. Dumitru AC, Poncin MA, Conrard L, Dufrêne YF, Tyteca D, Alsteens D, Nanoscale membrane architecture of healthy and pathological red blood cells, Nanoscale Horizons, 3 (2018) 293–304.

[60]. Alsteens D, Newton R, Schubert R, Martinez-Martin D, Delguste M, Roska B, Müller DJ, Nanomechanical mapping of first binding steps of a virus to animal cells, Nature Nanotechnology, 12 (2017) 177–183.

[61]. Kang L, Smith S, Wang C, Metal–Organic Framework Preserves the Biorecognition of Antibodies on Nanoscale Surfaces Validated by Single-Molecule Force Spectroscopy, ACS Applied Materials & Interfaces, 12 (2020) 3011–3020. [PubMed: 31846291]

[62]. Calzado-Martín A, Encinar M, Tamayo J, Calleja M, San Paulo A, Effect of Actin Organization on the Stiffness of Living Breast Cancer Cells Revealed by Peak-Force Modulation Atomic Force Microscopy, ACS Nano, 10 (2016) 3365–3374. [PubMed: 26901115]

[63]. van de Linde S, Löschberger A, Klein T, Heidbreder M, Wolter S, Heilemann M, Sauer M, Direct stochastic optical reconstruction microscopy with standard fluorescent probes, Nature Protocols, 6 (2011) 991–1009. [PubMed: 21720313]

[64]. Dempsey GT, Vaughan JC, Chen KH, Bates M, Zhuang X, Evaluation of fluorophores for optimal performance in localization-based super-resolution imaging, Nature Methods, 8 (2011) 1027–1036. [PubMed: 22056676]

[65]. Xu J, Ma H, Liu Y, Stochastic Optical Reconstruction Microscopy (STORM), Current Protocols in Cytometry, 81 (2017) 12.46.11–12.46.27. [PubMed: 28678417]

[66]. Fu PP, Xia Q, Hwang H-M, Ray PC, Yu H, Mechanisms of nanotoxicity: Generation of reactive oxygen species, Journal of Food and Drug Analysis, 22 (2014) 64–75. [PubMed: 24673904]

[67]. Xu Q, Huff LP, Fujii M, Griendling KK, Redox regulation of the actin cytoskeleton and its role in the vascular system, Free Radic Biol Med, 109 (2017) 84–107. [PubMed: 28285002]

[68]. García-Hevia L, Valiente R, Martín-Rodríguez R, Renero-Lecuna C, González J, Rodríguez-Fernández L, Aguado F, Villegas JC, Fanarraga ML, Nano-ZnO leads to tubulin macrotube assembly and actin bundling, triggering cytoskeletal catastrophe and cell necrosis, Nanoscale, 8 (2016) 10963–10973. [PubMed: 27228212]

[69]. Sasidharan A, Chandran P, Menon D, Raman S, Nair S, Koyakutty M, Rapid dissolution of ZnO nanocrystals in acidic cancer microenvironment leading to preferential apoptosis, Nanoscale, 3 (2011) 3657–3669. [PubMed: 21826307]

[70]. Manke A, Wang L, Rojanasakul Y, Mechanisms of Nanoparticle-Induced Oxidative Stress and Toxicity, BioMed Research International, 2013 (2013) 942916. [PubMed: 24027766]

[71]. Jiang X, Wu Y, Gray P, Zheng J, Cao G, Zhang H, Zhang X, Boudreau M, Croley TR, Chen C, Yin J-J, Influence of gastrointestinal environment on free radical generation of silver nanoparticles and implications for their cytotoxicity, NanoImpact, 10 (2018) 144–152.

[72]. Jiang X, Wang L, Ji Y, Tang J, Tian X, Cao M, Li J, Bi S, Wu X, Chen C, Yin J-J, Interference of Steroidogenesis by Gold Nanorod Core/Silver Shell Nanostructures: Implications for Reproductive Toxicity of Silver Nanomaterials, Small, 13 (2017) 1602855.

[73]. Luzuriaga MA, Benjamin CE, Gaertner MW, Lee H, Herbert FC, Mallick S, Gassensmith JJ, ZIF-8 degrades in cell media, serum, and some—but not all—common laboratory buffers, Supramolecular Chemistry, 31 (2019) 485–490. [PubMed: 31892768]

[74]. Strzelecka-Gołaszewska H, Pròchniewicz E, Drabikowski W, Interaction of actin with divalent cations. 1. The effect of various cations on the physical state of actin, European journal of biochemistry, 88 (1978) 219–227. [PubMed: 566667]

[75]. Brieher W, Mechanisms of actin disassembly, Mol Biol Cell, 24 (2013) 2299–2302. [PubMed: 23900650]

[76]. Doolittle LK, Rosen MK, Padrick SB, Measurement and analysis of in vitro actin polymerization, Methods Mol Biol, 1046 (2013) 273–293. [PubMed: 23868594]

[77]. Gu W, Bai X, Ren K, Zhao X, Xia S, Zhang J, Qin Y, Lei R, Chen K, Chang Y.-n., Zeng L, Li J, Xing G, Mono-fullerenols modulating cell stiffness by perturbing actin bundling, Nanoscale, 10 (2018) 1750–1758. [PubMed: 29308471]

[78]. Sharma S, Grintsevich EE, Phillips ML, Reisler E, Gimzewski JK, Atomic Force Microscopy Reveals Drebrin Induced Remodeling of F-Actin with Subnanometer Resolution, Nano Letters, 11 (2011) 825–827. [PubMed: 21175132]
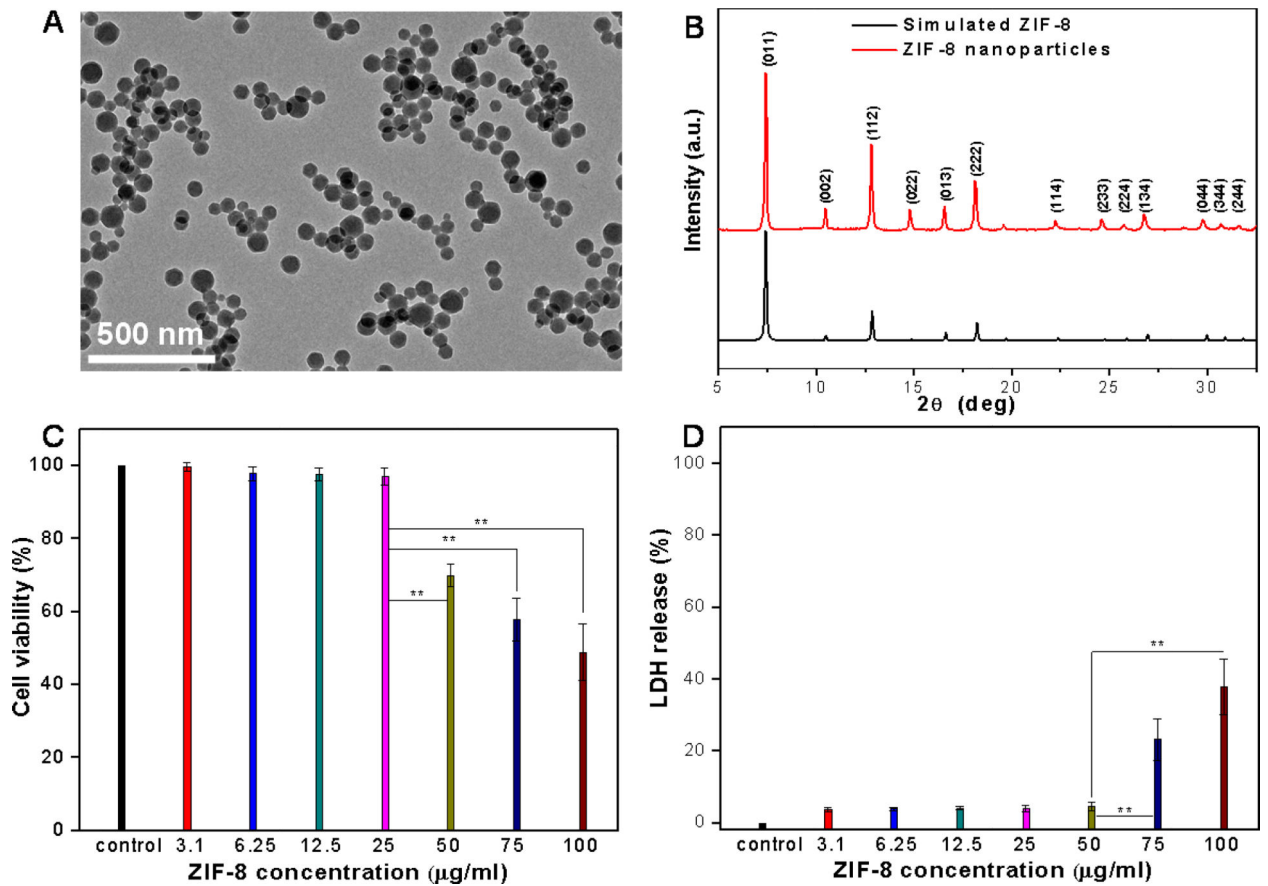
Figure 1.
(A) TEM image of synthesized ZIF-8 nanoparticles. (B) Powder XRD pattern of synthesized ZIF-8 nanoparticles and simulated powder XRD pattern of ZIF-8 (CCDC ID number: 864309). (C) MTT assay measuring VSMC viability after incubation with ZIF-8 nanoparticles for 24 h. (D) LDH assay measuring VSMC membrane integrity after incubation with ZIF-8 nanoparticles for 24 h. Data is mean ± standard deviation, n=6. Student's t-test, **P < 0.01.
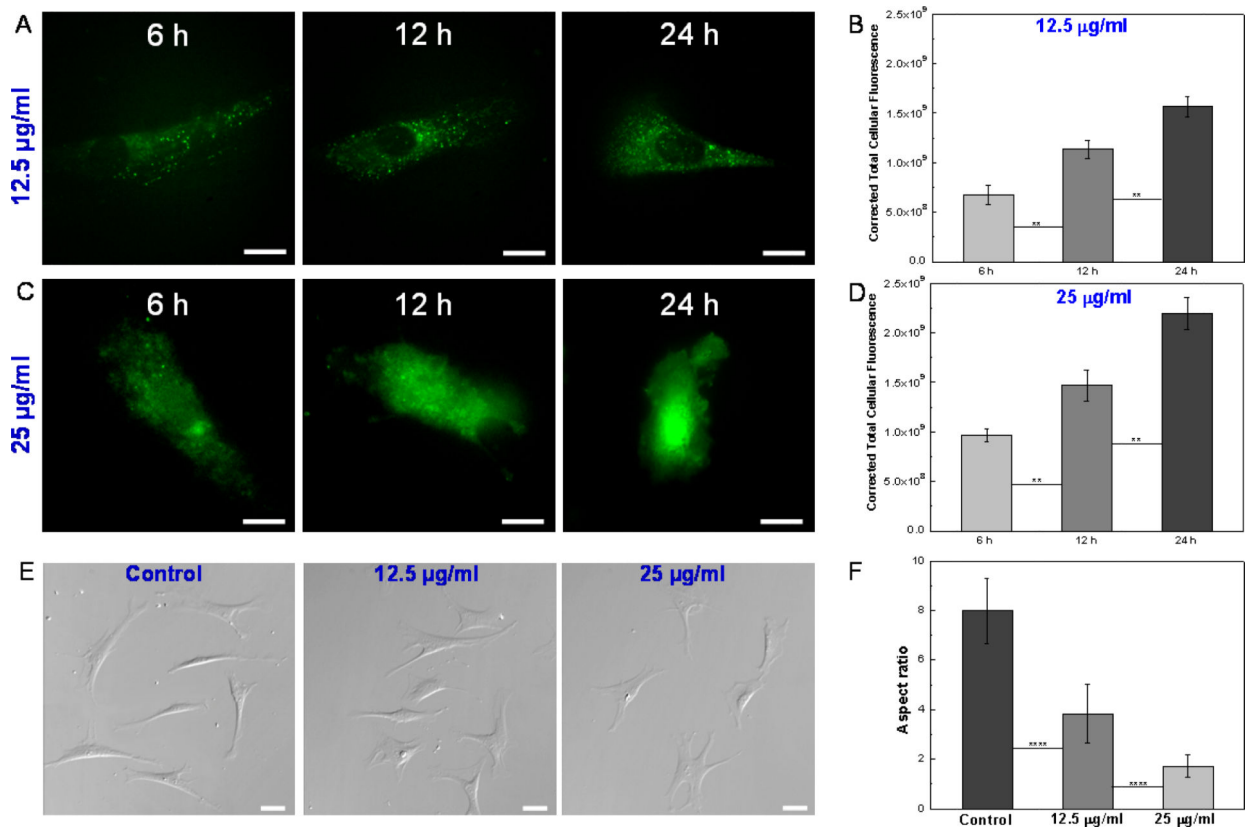
Figure 2.
(A) Fluorescence images of single VSMCs after incubation with 12.5 μg/ml FITC-loaded ZIF-8 nanoparticles for 6 h, 12 h and 24 h. Scale bars: 20 μm. (B) Quantitative analysis of cell uptake of 12.5 μg/ml ZIF-8 nanoparticles based on correlated total cell fluorescence (CTCF). Data is mean ± standard deviation, n=50. Student's t-test, **$P < 0.01$. (C) Fluorescence images of single VSMCs after incubation with 25 μg/ml FITC-loaded ZIF-8 nanoparticles for 6 h, 12 h and 24 h. Scale bars: 20 μm. (D) Quantitative analysis of cell uptake of 25 μg/ml ZIF-8 nanoparticles based on CTCF. Data is mean ± standard deviation, n=50. Student's t-test, **$P < 0.01$. (E) DIC images of VSMCs after incubation with 0 (control), 12.5 and 25 μg/ml ZIF-8 nanoparticles for 24 h. Scale bars: 40 μm. (F) Aspect ratios of VSMCs after incubation with 0 (control), 12.5 and 25 μg/ml ZIF-8 nanoparticles for 24 h. Data is mean ± standard deviation, n=100. Student's t-test, ****$P < 0.0001$. With the increase of ZIF-8 concentrations, the cells exhibited a less elongated, and more spread shape, leading to decreased aspect ratios.
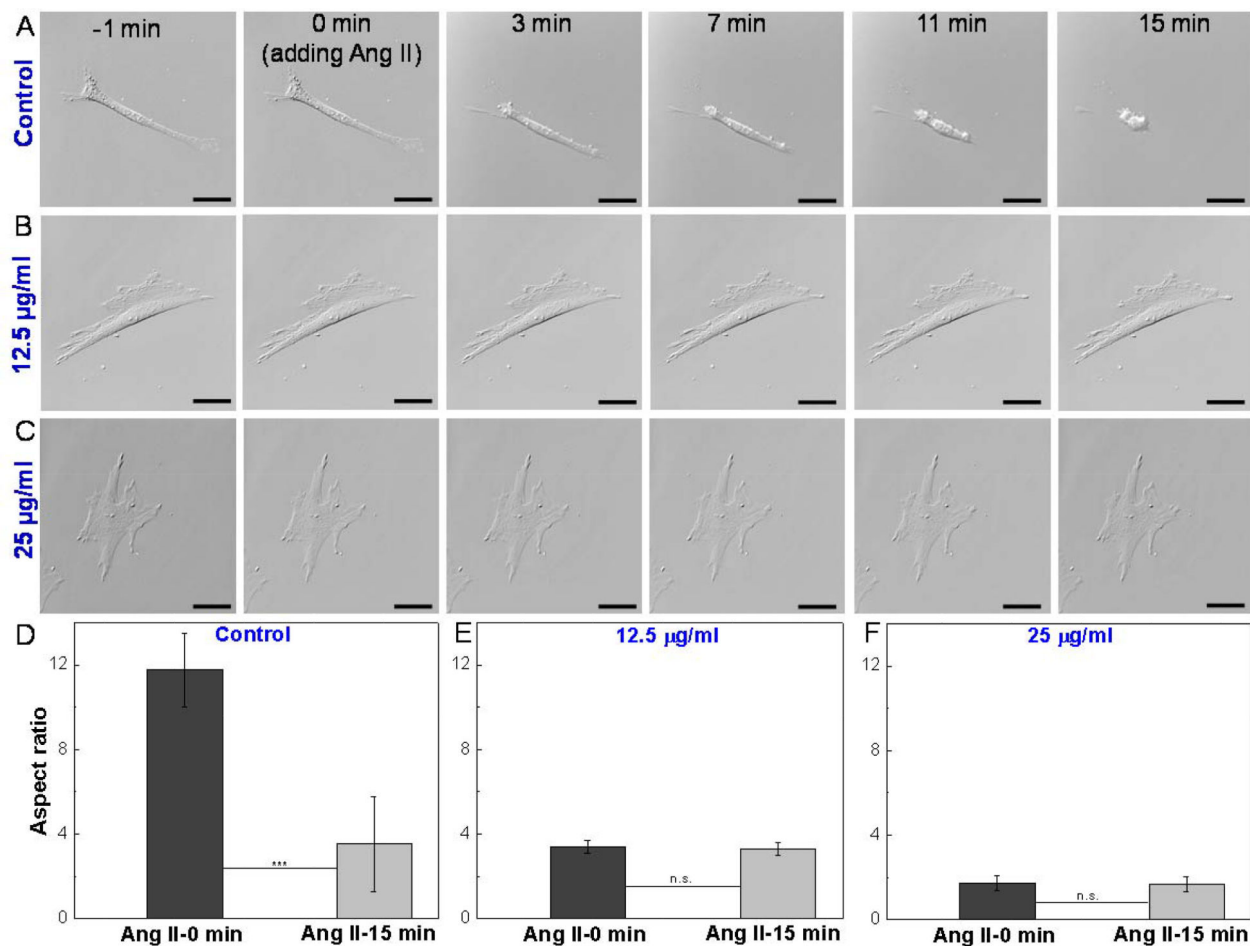
Figure 3.
Time-lapse DIC images of single VSMCs in response to Angiotensin II (Ang II) treatment. (A) Control: VSMC after incubation with standard medium for 24 h and subjected to Ang II treatment. (B) VSMC after incubation with 12.5 μg/ml ZIF-8 nanoparticles for 24 h and subjected to Ang II treatment. (C) VSMC after incubation with 25 μg/ml ZIF-8 nanoparticles for 24 h and subjected to Ang II treatment. Scale bars: 40 μm. (D-F) Aspect ratios of VSMCs before adding Ang II (0 min) and 15 min after adding Ang II. Data is mean ± standard deviation, n=10. Student's t-test, ***P < 0.001. Un-treated VSMCs (control) showed contraction in response to Ang II treatment, whereas ZIF-8 nanoparticle treated VSMCs lost contractility.
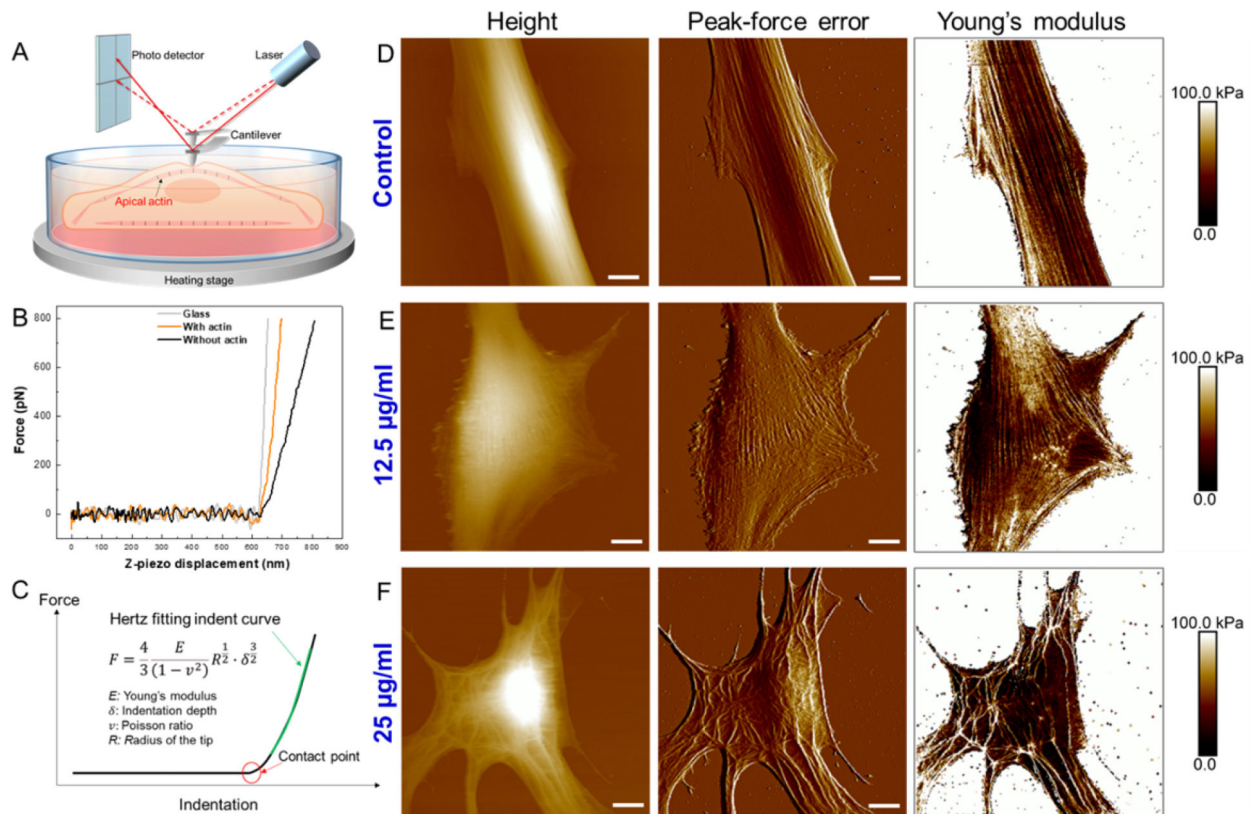
Figure 4.
(A) Schematic illustrating Peak-Force quantitative nanomechanical mapping of actin organization at the apical surfaces of live cells. (B) Raw force-displacement curves collected on glass, cell regions with apical actin filaments, and cell regions without apical actin filaments. (C) Hertz model fitting of force-indentation curve to obtain Young's modulus at each pixel. (D) Height, peak-force error and Young's modulus maps of single VSMC after incubation with 0 μg/ml (control) ZIF-8 nanoparticles for 24 h. (E) Height, peak-force error and Young's modulus maps of single VSMC after incubation with 12.5 μg/ml ZIF-8 nanoparticles for 24 h. (F) Height, peak-force error and Young's modulus maps of single VSMC after incubation with 25 μg/ml ZIF-8 nanoparticles for 24 h. Three types of maps showed excellent correlations to identify actin filaments at the apical surfaces of live cells. The ZIF-8 nanoparticles altered the VSMC morphology and actin organization in a concentration-dependent manner. Scale bars: 10 μm.
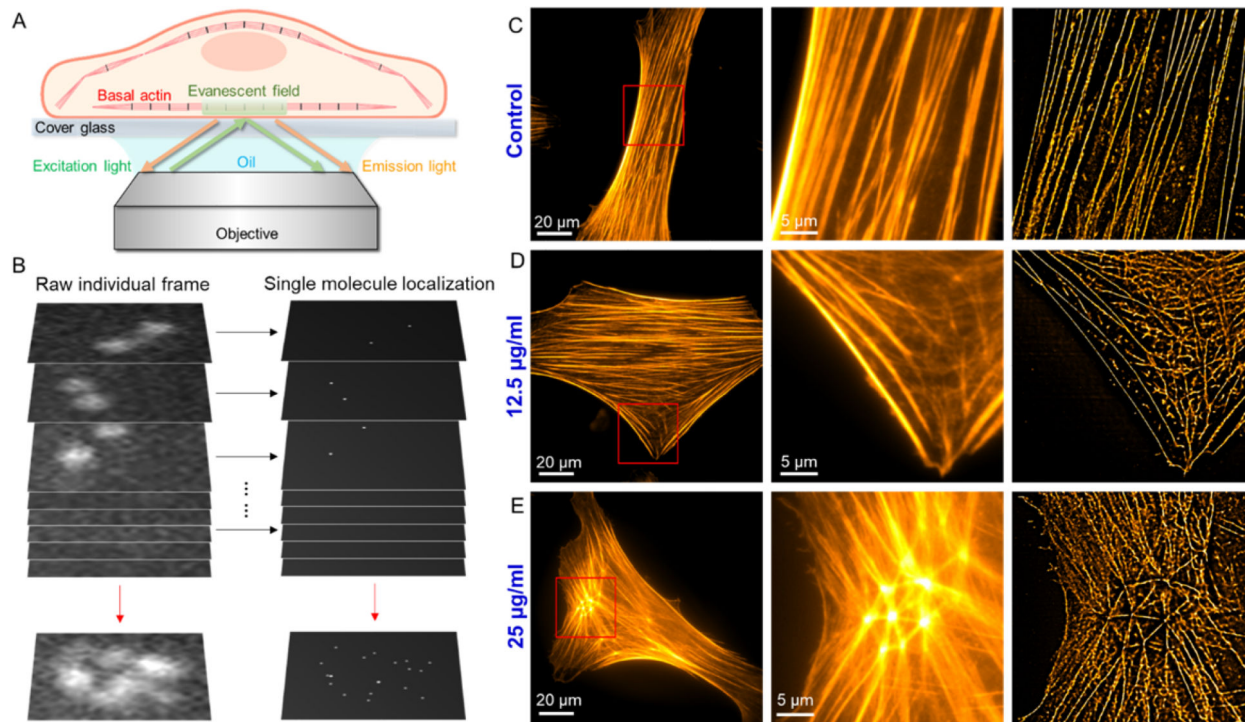
Figure 5.
(A) Schematic illustrating total internal reflection fluorescence (TIRF) imaging of actin organization at the basal surfaces of phalloidin fluorescence stained cells. (B) The concept of dSTORM: The super resolution image is obtained by localizing single molecules within a stack of >10,000 frames, each capturing a different subset of individual molecules from the total ensemble. (C-E) Epi-fluorescence image of single VSMCs, red-boxed area of the epi-fluorescence image, and dSTORM image of the same area: (C) Control: VSMC after incubation with 0 μg/ml ZIF-8 nanoparticles for 24 h. (D) 12.5 μg/ml: VSMC after incubation with 12.5 μg/ml ZIF-8 nanoparticles for 24 h. (E) 25 μg/ml: VSMC after incubation with 12.5 μg/ml ZIF-8 nanoparticles for 24 h. ZIF-8 nanoparticle treatment led to the formation of actin branches and networks at the basal layers of the cells.
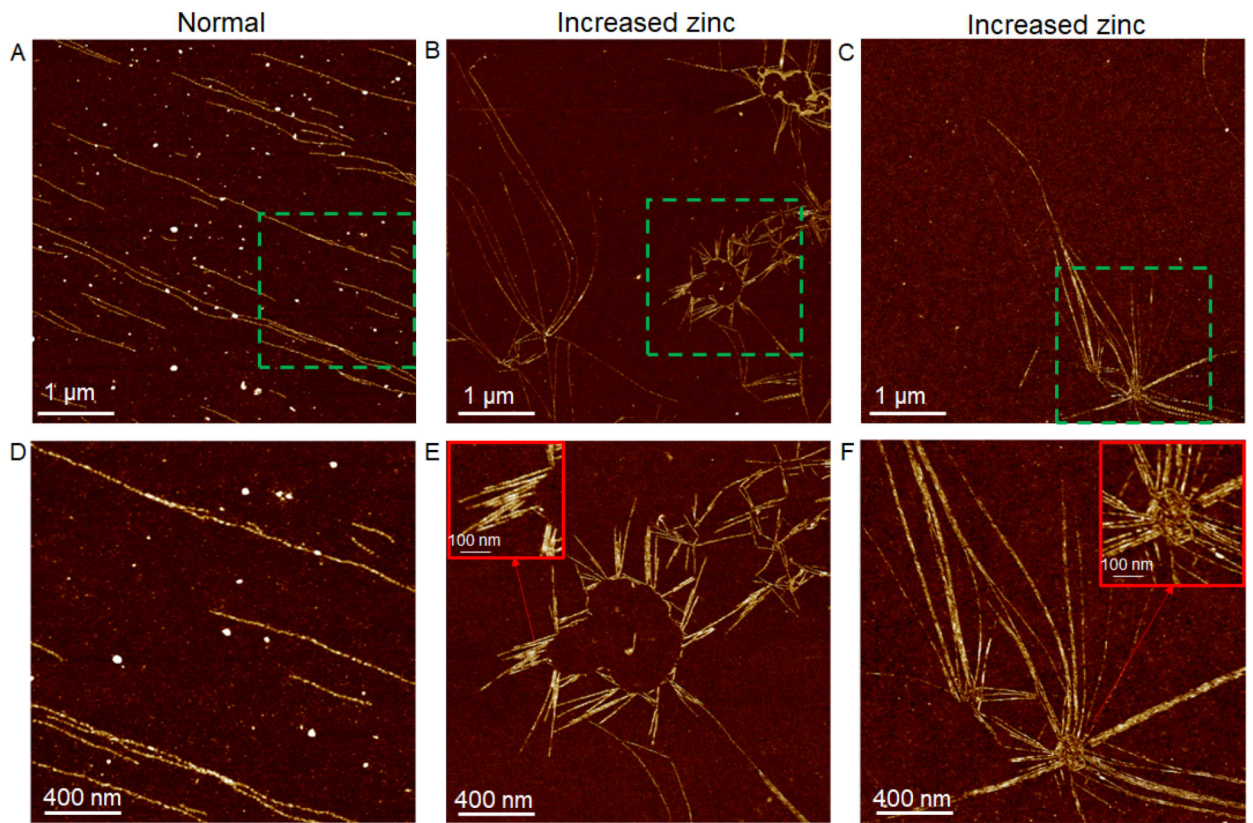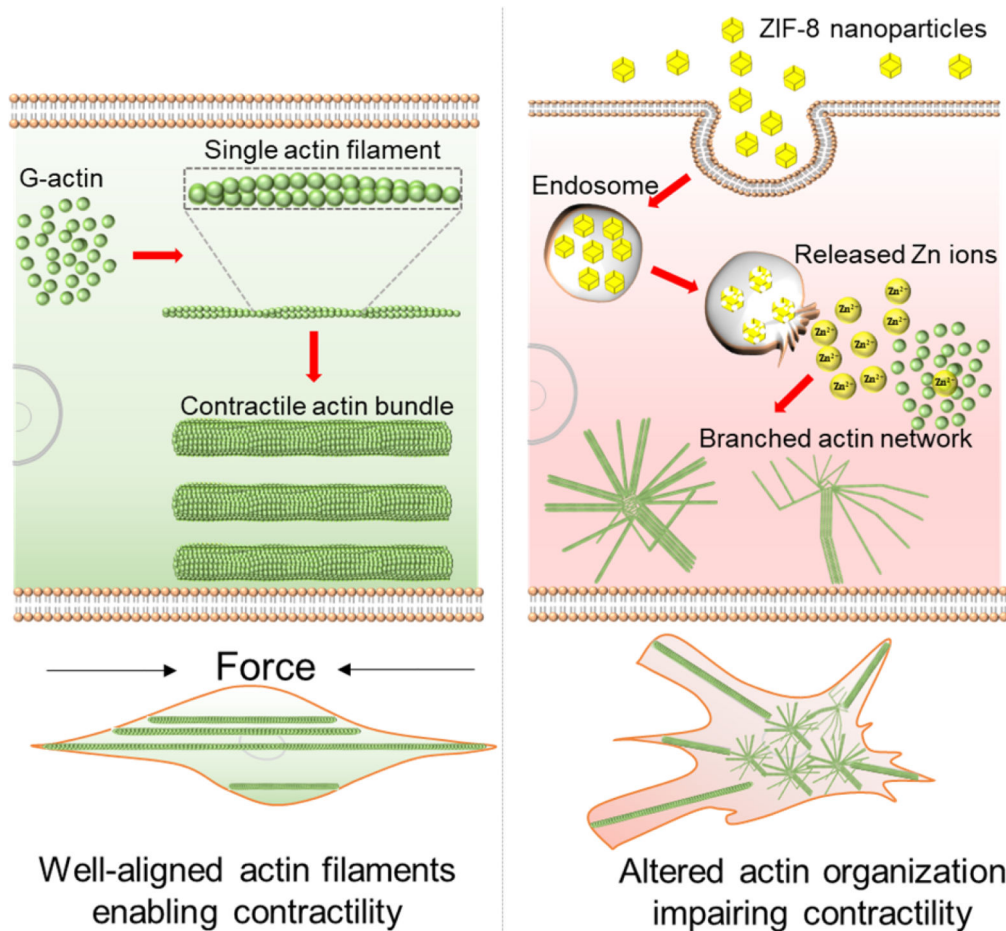
Figure 6.

Actin polymerization assay investigating the effect of increased Zn^{2+} on actin assembly process. (A) and (D): AFM images of single actin filaments assembled from G-actin under normal assay conditions. (B-C) and (E-F): AFM images of actin bundles, branches and networks assembled from G-actin in the presence of increased Zn^{2+} concentrations. D-F are enlarged images of green-boxed areas in A-C, respectively.

Figure 7.
Schematic illustrating how the ZIF-8 nanoparticles alter the actin organization in VSMCs. In the normal VSMCs (untreated cells), as shown in left column, G-actin assembles to single actin filaments, and then the filaments interact with actin-binding proteins such as myosin-II to form well-aligned actomyosin bundles, driving the contraction of cells. Upon uptake of ZIF-8 nanoparticles, as shown in right column, ZIF-8 nanoparticles dissolve in acidic endosomes/lysosomes and release Zn^{2+} into the cytoplasm, leading to increased intracellular Zn^{2+} levels. With increased intracellular Zn^{2+}, the G-actin directly assembles to actin bundles and networks, instead of linear, single actin filaments, during the actin polymerization process (as demonstrated in Figure 6). Essentially, the actin cytoskeleton remodeling process is likely impacted by the increased intracellular Zn2+ levels, thus hindering the formation of well-aligned contractile filaments (i.e., actomyosin bundles) and the contraction of VSMCs.